MiniMORPH: A Morphometry Pipeline for Low-Field MRI in Infants

Chiara Casella[a,b*], Aksel Leknes[c*], Niall J. Bourke[d], Ayo Zahra[c], Daniel Elijah Scheiene[c], Vanessa Kyriakopoulou[b], Simone R. Williams[e,f], Layla E. Bradford[e,f], Joanitta Murungi[g], Steven C.R. Williams[d], Sean C.L. Deoni[h], Victoria Nankabirwa[g, i], Kirsten A Donald[e,f], Muriel Marisa Katharina Bruchhage[c,l+], Jonathan O'Muircheartaigh[a,b,m+]

[a.] Department for Forensic and Neurodevelopmental Sciences, Institute of Psychiatry, Psychology and Neuroscience, King's College London, London, UK
[b.] Research Department of Early Life Imaging, School of Biomedical Engineering and Imaging Sciences, King's College London, London, UK
[c.] University of Stavanger, Institute of Social Sciences, Stavanger, Norway
[d.] Centre for Neuroimaging Sciences, Department of Neuroimaging, Institute of Psychiatry, Psychology & Neuroscience, Kings College London, UK
[e.] Department of Paediatrics and Child Health, Red Cross War Memorial Children's Hospital, University of Cape Town, Cape Town, South Africa
[f.] Neuroscience Institute, University of Cape Town, Cape Town, South Africa
[g.] Department of Epidemiology and Biostatistics, School of Public Health, College of Health Sciences, Makerere University, Kampala, Uganda
[h.] MNCH D&T, Bill & Melinda Gates Foundation, Seattle, WA, USA
[i.] Vilirana Hospital, Kampala, Uganda
[l.] Stavanger University Hospital, Stavanger Medical Imaging Laboratory, Department of Radiology, Stavanger, Norway
[m.] MRC Centre for Neurodevelopmental Disorders, King's College London, UK

*These authors contributed equally to this work.
[+]These authors share senior authorship.

Corresponding author:
Chiara Casella
Early Life Imaging, St Thomas' Hospital
King's College London
chiara.casella@kcl.ac.uk

Abstract

Background: Ultra-low-field (ULF) MRI facilitates neuroimaging access, yet its application in early infancy is constrained by low resolution/contrast, and the limited suitability of existing segmentation tools.

Objective: We present miniMORPH, an open-source pipeline for infant brain volumetry from 0.064T T2-weighted MRI scans. We evaluate its performance across multiple sites and ages and validate findings against high-field (HF) segmentations.

Methods: ULF scans were acquired from infants (2 to 27 months) across two cohorts in South Africa and Uganda. Age-specific templates and priors from established neurodevelopmental atlases were used to delineate brain tissues and substructures. Reliability was assessed by examining age, sex, and birthweight effects, and by comparing volumes to those from matched HF scans.

Results: miniMORPH successfully segmented major brain regions, capturing age-related growth trajectories. Sex-dependent volumetric differences were widespread but attenuated after intracranial volume correction. Low birthweight infants exhibited reduced regional volumes and altered growth trajectories. ULF-HF comparison showed strong correlations in most structures, although systematic biases were observed in ventricular estimates. Performance varied by age, with greatest segmentation deviation at 3 months.

Conclusion: miniMORPH enables reliable volumetric analysis of ULF infant MRI. Its compatibility with ULF systems supports equitable global neurodevelopmental research. The pipeline is openly available at https://github.com/UNITY-Physics/fw-minimorph.

1. Introduction

Infancy is a critical period for brain development, laying the foundation for future cognitive abilities (Bruchhage et al., 2020). MRI provides a powerful tool for visualising this maturation, offering quantitative measures predictive of both current and future cognitive outcomes (Abate et al., 2024). However, access to MRI in low- and middle-income countries (LMICs) remains extremely limited, restricting research capacity and the ability to capture neurodevelopmental variability in these settings (Abate et al., 2024).

Recent advances in portable, ultra-low-field (ULF) MRI (0.064T) offer a promising solution to this challenge. These systems are substantially more affordable (□$200,000–400,000 compared to $1.5–4 million for conventional MRI), require far less power (similar to that of a household appliance), and produce a small fringe field, making them suitable for use in clinical wards or community research centres without the need for extensive magnetic or radiofrequency shielding. Overall, their portability, low acoustic noise, and ease of installation make ULF systems highly feasible for deployment in resource-constrained environments and paediatric imaging, positioning them as a transformative technology for global developmental imaging accessibility (Abate et al., 2024).

By enabling the acquisition of MRI data in settings where it was previously inaccessible, ULF imaging could significantly advance our understanding of neurodevelopment, particularly in relation to environmental and genetic factors that require large, diverse cohorts to investigate effectively. One such factor is birthweight, a robust marker of early-life health that has been linked to differences in brain volume and structure across childhood (de Kieviet et al., 2012; Walhovd et al., 2012). This is especially relevant in LMICs, where challenges such as malnutrition, infection, and environmental hardship can be more prevalent and could influence early brain development. Addressing this gap is critical, as fewer than 3% of available neuroimaging data originates from LMICs, with even fewer studies including children beyond the neonatal period (Rutherford et al., 2022). Consequently, the impact of early-life adversity in these regions remains poorly understood, limiting the generalisability of findings derived from studies conducted primarily in North America, Europe, and Australia. Despite its potential, the application of ULF MRI in neonatal and paediatric populations is limited. To date, only a handful of studies have investigated ULF imaging in these groups (S. C. Deoni et al., 2021; Sabir et al., 2023; Tu et al., 2023). Importantly, the combination of low anatomical contrast in the infant brain and the lower image resolution and signal-to-noise ratio (SNR) inherent to ULF MRI presents challenges for the application of existing morphometric tools (Donnay et al., 2024). Addressing these limitations is essential for realising the full potential of ULF MRI to support global neurodevelopmental research.

In this work, we present miniMORPH, a pipeline for reliably quantifying brain tissue volumes from 0.064T MRI data acquired across infancy, enabling automatic segmentation of low-resolution T2-weighted (T2-w) data. We demonstrate the miniMORPH's reliability by revealing age, sex, and birthweight-related differences in brain growth over the first two years of life. We also quantitatively compare the pipeline's performance to regional volumes obtained from validated segmentation methods applied to paired high-field images. Open-source and cloud-integrated, the pipeline unlocks new possibilities for assessing neurodevelopment in diverse settings, offering a scalable solution compatible with ULF imaging platforms.

2. Methods

2.1. Acquisition:

The data used in this study were acquired at the University of Cape Town (UCT-Khula study) and at Makerere University & Kawempe Referral Hospital (KRH), Kampala (Uganda-PRIMES study), on the Hyperfine Swoop system (Abate et al., 2024) (Acquisition details are shown in Figure 1). The Makerere University School of Public Health Higher Degrees Research and Ethics Committee (REC reference No: 871) and the Uganda National Council for Science and Technology (UNCST reference No: HS1226ES) provided ethical approval for the Uganda-PRIMES study. The UCT-Khula study received ethical approval from the University of Cape Town Human Ethics Research Committee (HREC; 666/2021). All mothers provided written informed consent for their children.

2.2. Analysis:

Computation of T2-w isotropic volumes:
Isotropic images to be segmented were produced from three anisotropic T2-w acquisitions by first resampling the axial T2-w images to 1.5mm isotropic voxels using FLIRT (Jenkinson et al., 2012) and by then using the Advanced Normalization Tools (ANTs) template construction pipeline (Avants et al., 2011) on the three anisotropic images (Deoni et al., 2022).

Age-specific template construction:
Templates for the 3-, 6-, 12-, 18-, and 24-month age points were constructed using a subset of high-quality, low-motion ULF datasets from the UCT-Khula cohort. Specifically, mri_synthstrip (Hoopes et al., 2022) was first used to brain-extract the isotropic T2-w images. FSL (fslmaths) was used to generate edge (gradient) images. Brain-extracted and edge images were then used to create multi-channel templates in ANTs (Avants et al., 2011).

Creation of age-specific templates and priors
Tissue and cerebrospinal fluid (CSF) priors were generated by registering T2-w images from the Baby Connectome Project (BCP) atlas (Chen et al., 2022) at 3, 6, 12, 18, and 24 months to the study templates using SynthMorph (Hoffmann et al., 2024). White matter (WM), grey matter (GM), and cerebrospinal fluid (CSF) probability maps were transformed accordingly. A “tissue” prior was created by combining WM and GM maps, and a "skull" prior was generated by dilating the brain mask for improved classification of non-brain regions.

To generate subcortical GM masks, age-specific templates were first resampled to 0.5mm isotropic resolution. The subcortical parcellation maps from the Baby Connectome Project (BCP) atlas (Chen et al., 2022) were then registered to the 12-month template using the ANTs SyN algorithm (Avants et al., 2011). Thalamus and caudate masks were manually refined on the 12-month template to ensure anatomical accuracy. All resulting masks were subsequently propagated to the remaining age-specific templates using a series of non-linear transformations computed via ANTs.

To obtain callosal parcellations, the callosum mask from the Penn-CHOP Atlas (Song et al., 2024) was first registered to the 12-month template. Manual segmentation of the corpus callosum was then performed on the 12-month template, guided by anatomical landmarks

corresponding to the Desikan-Killiany atlas subdivisions (Desikan et al., 2006). The resulting parcellated mask was reviewed for anatomical accuracy and subsequently propagated to the remaining age-specific templates using the same ANTs-based transformation framework applied to the subcortical GM masks.

Ventricles, cerebellum, and brainstem masks were manually delineated in template space and reviewed by an expert. Here, region-specific strategies were employed to optimise segmentation reliability. Specifically, ventricles masks were drawn on each age-specific template, while brainstem and cerebellum masks were initially defined in the 12-month template space and then propagated to the younger and older template spaces via intermediate templates (e.g., from 12-month to 24-month via the 18-month template).

Individual segmentation and atlasing

For segmentation, T2-w isotropic images were registered to the appropriate age-specific template using ANTs, and the inverse transformations were applied to resample tissue priors into native space. Segmentation into the three primary tissue classes (tissue, CSF and skull) was performed using ANTs Atropos (Avants et al., 2011), with a prior probability weighting of 0.5.

To refine the segmentation, the CSF tissue class was multiplied by the ventricle mask, enabling the separation of ventricular CSF from extra-ventricular CSF; the subcortical GM mask was used to isolate subcortical grey matter from the overall tissue class; the brainstem and cerebellum masks were multiplied with both the tissue posterior and the CSF posterior in native space. This allowed us to separate supratentorial tissue from brainstem and cerebellar tissue, and likewise to distinguish supratentorial CSF from CSF within the posterior fossa.

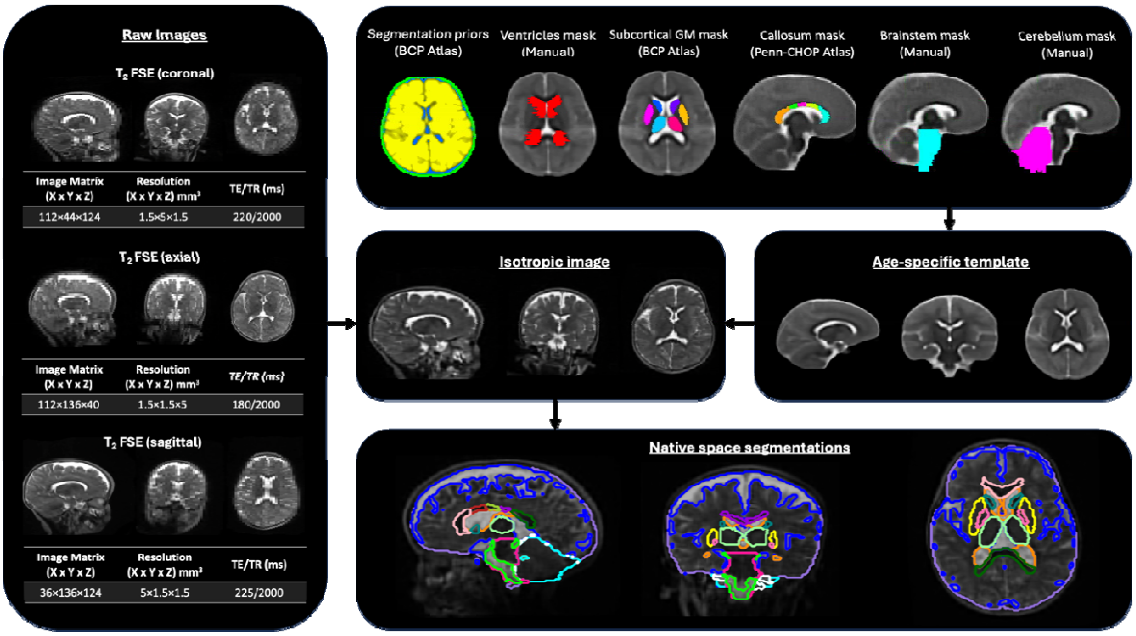

Figure 1. Summary diagram of the segmentation pipeline. *The pipeline begins with raw T2-w MRI images acquired in multiple orientations, which are processed to create an isotropic image. Segmentation priors from the BCP atlas (Chen et al., 2022), along with segmentation masks from the BCP and Penn-CHOP atlas (Song et al., 2024), are then aligned to native space through an age-specific template for segmentation.*

Quality control (QC):
QC of segmentation volumes was performed using outlier analysis against an age-group statistics. Subjects with greater than ±2 standard deviations in any of the segmented areas were flagged and checked. Participants with poor quality data and segmentations were excluded.

Effect of age and sex:
The pipeline's face validity was assessed by examining the effect of age and sex on brain volumes in the UCT-Khula dataset, using mixed-effects regression models. Model selection used the Bayesian Information Criterion (BIC) (Schwarz, 1978) to determine if a quadratic or linear model best fit each volume. All volumes were plotted against age in months, with and without correction for intracranial volume (ICV, calculated as the sum of supratentorial tissue, supratentorial CSF, cerebellum tissue, cerebellum CSF, brainstem tissue and brainstem CSF.

Effect of birthweight:
The effect of birthweight - categorized as low (Uganda-PRIMES) versus normal (UCT-Khula) - on brain tissue volumes was assessed using linear mixed models fitted separately for uncorrected and ICV-corrected regional volumes, with fixed effects for group (low vs. normal birthweight), age in months, their interaction, and sex. The UCT-Khula dataset was restricted to participants aged 2-14-months to match sampling and age to the Uganda-PRIMES dataset. To account for multiple comparisons across brain regions, Bonferroni correction was applied to all p-values.

Quantitative comparison of segmentation volumes between high-field and ULF MRI
For the validation of miniMORPH results, the volumes were compared with matched HF scans (Uganda-PRIMES:1.5T; UCT-Khula: 3T). Matched HF scans were obtained within ±90 days of the ULF scan, with a mean absolute difference ranging from approximately 1 to 29 days across age groups. The average interval was typically under one month, highlighting the close temporal alignment of the paired acquisitions. Notably, the gap between scans was narrowest at the youngest age points, ensuring minimal developmental change between modalities at these critical early stages. In total, there were 193 instances of matched HF and ULF scans, and their age, cohort distribution and mean difference in exact age as well as scanner and sequence information are shown in table 1. To estimate correspondence with validated methods, HF segmentations were obtained using SynthSeg, which has proven high performance variety of contrasts and resolutions (Billot et al., 2023).

To assess the pipeline performance, the error between paired HF and ULF volumes was measured. To enable comparison of performance across regions, the paired error was standardized by HF estimates, resulting in a relative measure for every paired volume. for standardization, as they were expected to be the closest to "true" volumes. By standardizing, the performance of miniMORPH for large regions, such as supratentorial tissue, can be compared to smaller regions. The error metric, percentage error (PE), was calculated for each matching ROI as:

$$PE = \frac{(v_{HF} - v_{ULF})}{v_{HF}} \cdot 100\%$$

Due to differences in exact age between HF and ULF, a corrected relative difference was calculated. This was done using the slope, s, of a linear regression with time between HF and ULF scans as independent variable and PE as dependent variable. Although brain development in early life is known to follow a non-linear trajectory, the timescale under consideration here - typically less than one month - is sufficiently short to justify the use of a linear approximation. Corrected percentage error (CPE) was then calculated as:

$$CPE = s \cdot \Delta t \cdot PE$$

In addition to CPE, correlation was calculated for each region at all ages. While CPE gives an estimate of the relative error expected for each ROI, correlation gives an indication of how well differences between HF scans are represented in ULF.

Both CPE and correlation was investigated for all matched UCT-Khula and Uganda-PRIMES subjects. Furthermore, to investigate the difference in performance across cohort, CPE and correlation for 12 months old subjects from UCT-Khula and Uganda-PRIMES were compared. Lastly, miniMORPH performance at different ages were analysed by stratifying correlation and CPE across 3, 6, 12, 18 and 24 months for all matched HF and ULF scans in the UCT-Khula cohort.

	Uganda-PRIMES	**UCT-Khula**				
Scanner	Siemens Sempra	Siemens Skyra				
Sequence	T1-w MPRAGE	T2-w				
Field strength	1.5T	3T				
Image matrix (X × Y × Z)	256 × 256 × 192	256 × 256 × 144				
Resolution (X × Y × Z) mm^3	0.95 × 0.9766 × 0.9766	1 × 1 × 1				
Matched age (Months)	**12**	**3**	**6**	**12**	**18**	**24**
Participants	41 (27F)	33 (17F)	45 (15F)	42 (17F)	15 (5F)	7 (3F)
Days between HF and ULF scan (μ)	12.90	-1.18	28.71	24.48	27.2	-64.43

Table 1: Cohort specifications for Uganda-PRIMES and UCT-Khula with HF scanner specifications and matched participants.

3. Results

QC:

The percentage of excluded segmentations for each brain region and template age is summarised in Table 2, stratified by cohort. Exclusions varied across regions and ages, with a greater number of excluded segmentations observed at younger ages. Table 3 shows the sample demographics for each cohort, after QC. Figures 2 and 3 display segmentation results in a representative subject, with Figure 2 illustrating whole-brain performance and Figure 3 highlighting longitudinal changes in callosal segments (top row) and subcortical grey matter (bottom row) across timepoints.

Table 2. Percentage of segmentations excluded following QC, by template age and cohort. *Segmentations were assessed on a region-by-region basis within each subject.*

Region	**Template Age**				
UCT-Khula					
	3M	**6M**	**12M**	**18M**	**24M**
Supratentorial tissue	7.0%	4.4%	2.6%	12.2%	4.5%
Supratentorial CSF	7.6%	4.4%	2.6%	12.2%	4.5%
Ventricles	7.6%	3.9%	2.6%	9.8%	3.4%
Cerebellum	8.3%	6.9%	7.2%	21.9%	4.5%
Cerebellum CSF	8.3%	6.9%	7.8%	21.9%	4.5%
Brainstem	8.3%	7.4%	7.2%	21.9%	4.5%
Brainstem CSF	8.3%	6.9%	7.8%	21.9%	4.5%
Left thalamus	7.6%	3.9%	2.6%	9.8%	3.4%
Left caudate	7.6%	3.9%	2.6%	9.8%	3.4%
Left putamen	7.6%	3.9%	2.6%	9.8%	3.4%
Left globus pallidus	7.6%	3.9%	2.6%	9.8%	3.4%
Right thalamus	7.6%	3.9%	2.6%	9.8%	3.4%
Right caudate	7.6%	3.9%	2.6%	9.8%	3.4%
Right putamen	7.6%	3.9%	2.6%	9.8%	3.4%
Right globus pallidus	7.6%	3.9%	3.3%	9.8%	3.4%
Posterior callosum	8.3%	3.9%	3.3%	9.8%	3.4%
Mid-posterior callosum	8.3%	4.4%	6.5%	12.2%	4.5%
Central callosum	7.6%	3.9%	4.6%	12.2%	4.5%
Mid anterior callosum	7.6%	4.9%	2.6%	14.6%	4.5%
Anterior Callosum	7.6%	6.4%	3.9%	14.6%	3.4%
Uganda-PRIMES					
Supratentorial tissue	11.5%	23.5%	13.4%	-	-
Supratentorial CSF	11.5%	23.5%	13.4%	-	-
Ventricles	11.5%	23.5%	14.9%	-	-
Cerebellum	11.5%	23.5%	13.4%	-	-
Cerebellum CSF	11.5%	23.5%	13.4%	-	-
Brainstem	11.5%	23.5%	13.4%	-	-
Brainstem CSF	11.5%	23.5%	13.4%	-	-
Left thalamus	11.5%	25.0%	13.4%	-	-

Left caudate	11.5%	25.0%	13.4%	-	-
Left putamen	11.5%	23.5%	13.4%	-	-
Left globus pallidus	11.5%	23.5%	13.4%	-	-
Right thalamus	11.5%	25.0%	13.4%	-	-
Right caudate	11.5%	26.5%	13.4%	-	-
Right putamen	11.5%	23.5%	13.4%	-	-
Right globus pallidus	11.5%	23.5%	13.4%	-	-
Posterior callosum	11.5%	23.5%	13.4%	-	-
Mid-posterior callosum	11.5%	23.5%	13.4%	-	-
Central callosum	11.5%	23.5%	13.4%	-	-
Mid anterior callosum	11.5%	27.9%	13.4%	-	-
Anterior Callosum	11.5%	27.9%	13.4%	-	-

Table 3. Sample demographics after QC for each cohort.

Uganda-PRIMES	
Mean Age/Age-range (Months)	8.2/2-14
Template Age Bins (Count)	3M: 19 6M: 52 12M: 58
Sex (Count)	19 Male, 25 Female
Subjects with Longitudinal Data	44
UCT-Khula	
Mean Age /Age-range (Months)	10.77/2–27
Template Age Bins (Count)	3M: 105 6M: 127 12M: 174 18M: 87 24M: 23
Sex (Count)	108 Male, 96 Female
Subjects with Longitudinal Data	194

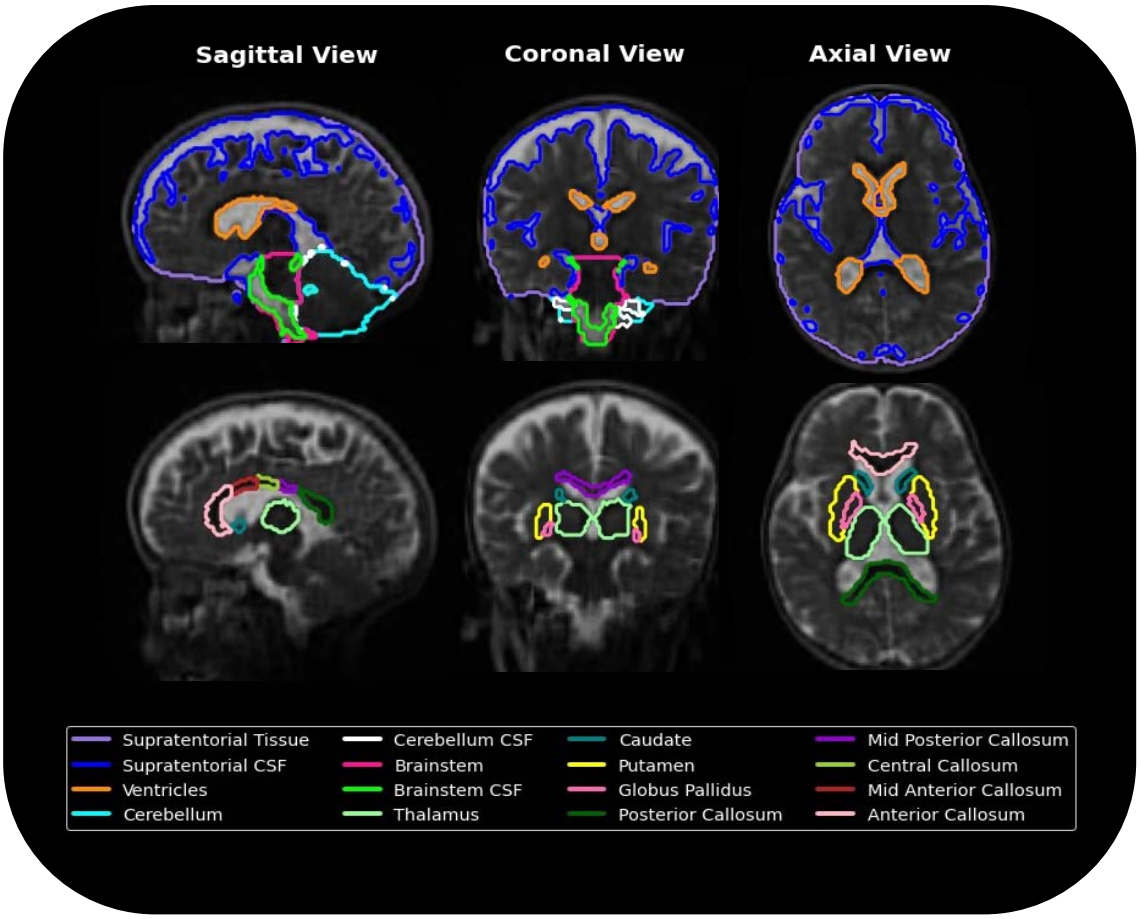

Figure 2. Example segmentation results across sagittal, coronal, axial views. *Each view highlights key anatomical structures, demonstrating the detailed parcellation of supratentorial and infratentorial structures critical for volumetric and morphological analysis.*

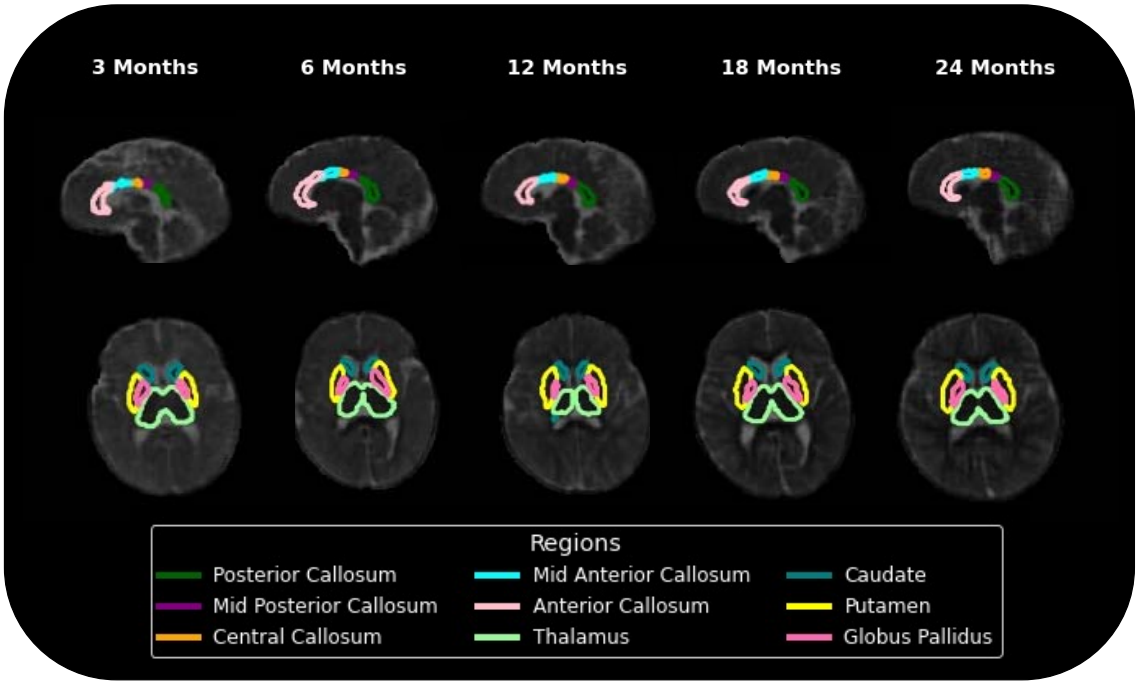

Figure 3. Segmentation results for callosal segments (top row) and subcortical GM (bottom row) on one representative subject using age-matched templates (template ages shown). *Developmental changes in brain regions over time can be observed, reflecting sensitivity of the pipeline to structural maturation during early infancy.*

Effect of age and sex on brain morphometry

Age and sex effects for both uncorrected and ICV-corrected volumes are plotted in Figure 4 and detailed in Table 4.

Nearly all regions exhibit significant positive linear effects of age. Quadratic age terms are significantly negative across most regions, especially in the cerebellum, CSF spaces, and callosal subregions, suggesting nonlinear growth curves with early acceleration and later deceleration. Notably, the thalamus and caudate fit a linear model with a strong age effect and no significant quadratic age term — consistent with more stable linear growth.

After correcting for ICV, age effects in supratentorial tissue become non-significant ($p=0.18$), likely due to the supratentorial region constituting a large proportion of total ICV. The quadratic term remains marginally significant. On the other hand, the cerebellum retains highly significant age and age^2 effects post-ICV correction, showing continued region-specific maturation beyond global size scaling. Likewise, the thalamus, globus pallidus and caudate also retain strong age effects after ICV correction, suggesting these structures undergo meaningful development in volume even when overall brain size is accounted for.

Although highly significant in uncorrected models, most callosal regions show reduced or non-significant age effects after correction. The mid-anterior and anterior callosum remain significant for age and age^2, consistent with regionally specific shape and thickness changes observed in neonatal callosal development.

While sex has robust effects throughout most of the brain for uncorrected volumes — most prominently in supratentorial tissue, cerebellum, and posterior corpus callosum — with males typically having larger regional volumes, as expected, many sex differences are attenuated or eliminated after adjusting for ICV, indicating that most regional differences are proportional to overall brain size.

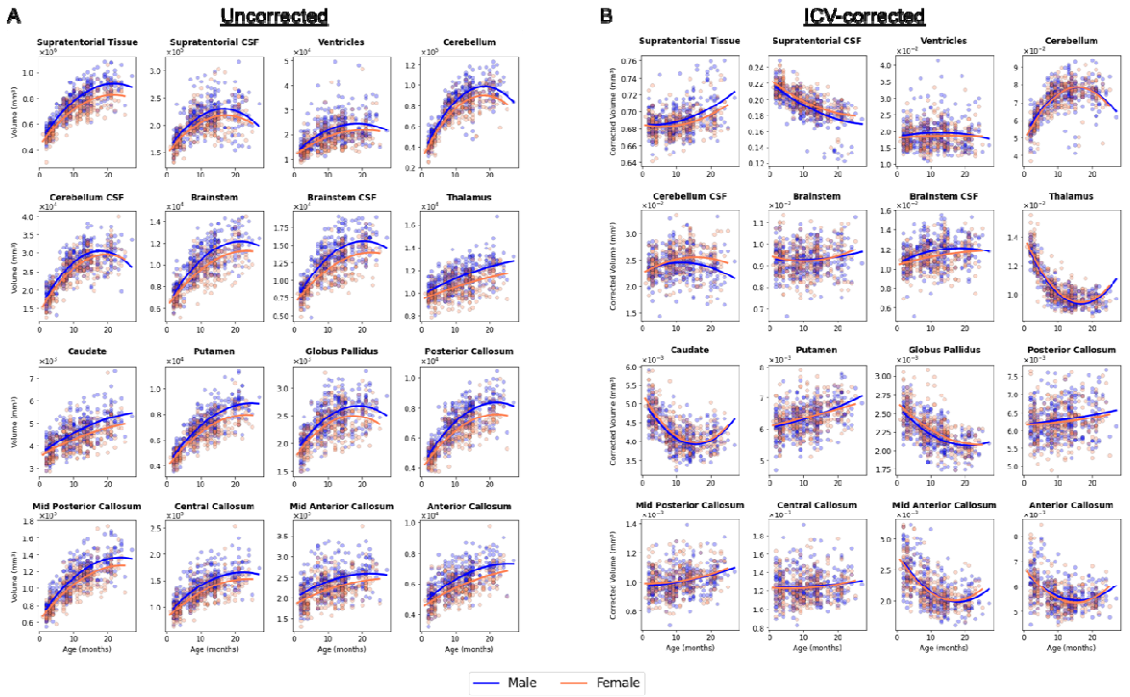

Figure 4. Effect of age and sex on brain volumes*. A) Absolute volumes. B) Volumes corrected for ICV. The datapoints represent individual measurements. For each brain region and sex, we compared linear and quadratic regression models using the coefficient of determination (R^2) as a measure of model fit. The model with the higher R^2 was selected and used to generate fitted curves.*

Table 4. Summary results of the mixed-effects models assessing the effect of age and sex on regional brain volumes.

Uncorrected						
Region	**Sex Effect**	**Corrected p (Sex)**	**Age Effect**	**Corrected p (Age)**	**Quadratic Age Effect (p-value)**	**Corrected p (Age^2)**
Supratentorial tissue	63183.9614	**2.68E-26**	39117.4968	**7.12E-96**	-892.7499	**3.40E-30**
Supratentorial CSF	10214.0069	**1.26E-06**	8791.06053	**5.63E-45**	-259.3807	**1.20E-23**
Ventricles	2366.81877	**3.96E-08**	1206.84906	**3.48E-20**	-31.296255	**2.71E-08**
Cerebellum	7053.71233	**4.26E-16**	7231.26777	**1.88E-163**	-197.21719	**2.91E-73**
Cerebellum CSF	1309.15432	**1.46E-06**	1692.70515	**4.77E-103**	-45.808409	**1.61E-45**
Brainstem	782.941131	**1.50E-15**	496.848946	**9.70E-60**	-11.079133	**3.98E-18**

Brainstem CSF	1472.71826	**3.09E-21**	769.7384	**1.99E-56**	-18.192016	**3.52E-19**
Thalamus	728.780705	**1.47E-19**	107.058132	**2.16E-60**		1
Caudate	282.325646	**6.08E-11**	100.165797	**2.50E-13**	-1.3969815	0.13967485
Putamen	520.590705	**2.52E-14**	371.001492	**2.53E-69**	-7.6235112	**6.79E-18**
Globus pallidus	130.705346	**6.51E-09**	91.1647054	**4.61E-41**	-2.5102742	**6.76E-19**
Posterior callosum	589.524984	**1.47E-19**	364.310847	**1.53E-68**	-8.2974108	**1.21E-21**
Mid-posterior callosum	76.7037258	**6.56E-12**	57.3489501	**3.81E-63**	-1.1905914	**1.25E-16**
Central callosum	117.452057	**1.72E-11**	68.3637674	**2.13E-37**	-1.4867587	**7.99E-11**
Mid-anterior callosum	182.547097	**3.02E-11**	49.9692895	**2.83E-08**	-1.0168306	**0.04515241**
Anterior callosum	493.51014	**5.73E-14**	182.569712	**1.12E-18**	-3.2440844	**0.00115071**
ICV-corrected						
Supratentorial tissue	0.00443259	**0.01142901**	-0.0005605	1	6.70E-05	**0.00151859**
Supratentorial CSF	-0.0053064	**1.35E-05**	-0.0034477	**3.66E-22**	5.97E-05	**0.00039885**
Ventricles	0.00076109	0.3123177	1.39E-05	1		1
Cerebellum	0.00064017	1	0.00364034	**9.26E-90**	-0.000115	**6.23E-54**
Cerebellum CSF	-0.0006557	0.055598	0.00033732	**3.90E-05**	-1.27E-05	**0.0002275**
Brainstem	-1.84E-05	1	7.64E-06	1		1
Brainstem CSF	0.00047016	**0.00062178**	6.18E-05	**8.47E-10**		1
Thalamus	-0.0001369	0.19132756	-0.0005496	**3.19E-215**	1.64E-05	**2.37E-115**
Caudate	-7.34E-05	0.13909017	-0.0001628	**1.91E-72**	5.18E-06	**3.40E-44**
Putamen	-2.48E-05	1	3.22E-05	**8.96E-24**		1
Globus pallidus	-5.50E-05	**0.00408543**	-4.97E-05	**7.32E-24**	1.11E-06	**2.53E-07**
Posterior callosum	6.15E-05	1	1.30E-05	**0.001245**		1
Mid-posterior callosum	-7.32E-06	1	4.03E-06	**3.13E-09**		1
Central callosum	1.61E-05	1	2.24E-06	0.5562203		1
Mid-anterior callosum	7.64E-06	1	-8.91E-05	**4.26E-42**	2.55E-06	**9.94E-21**
Anterior callosum	3.60E-05	1	-0.0001639	**4.19E-29**	5.29E-06	**2.14E-18**

Relationship between brain morphometry and birthweight

Birthweight effects for both uncorrected and ICV-corrected volumes are plotted in Figure 5 and detailed in Table 5.

Significant effects of birthweight group were observed in multiple brain regions. In uncorrected models, children born with low birthweight exhibited increased CSF volumes and reduced tissue volumes in regions including the supratentorial compartment, cerebellum, caudate, and putamen ($p < 0.001$). These group differences remained statistically significant after ICV correction in selected regions, notably the cerebellum and caudate, indicating localised volumetric alterations not fully attributable to global brain size.

Age-by-group interaction effects were detected in regions such as the cerebellum, thalamus, and corpus callosum, suggesting that developmental trajectories differ by birthweight status. In these regions, volumes in the low birthweight group showed divergent age-related patterns, consistent with atypical or delayed postnatal growth. Age-related increases in brain volume were widespread across the cohort, but birthweight-specific effects and interactions were prominent in both subcortical and callosal structures.

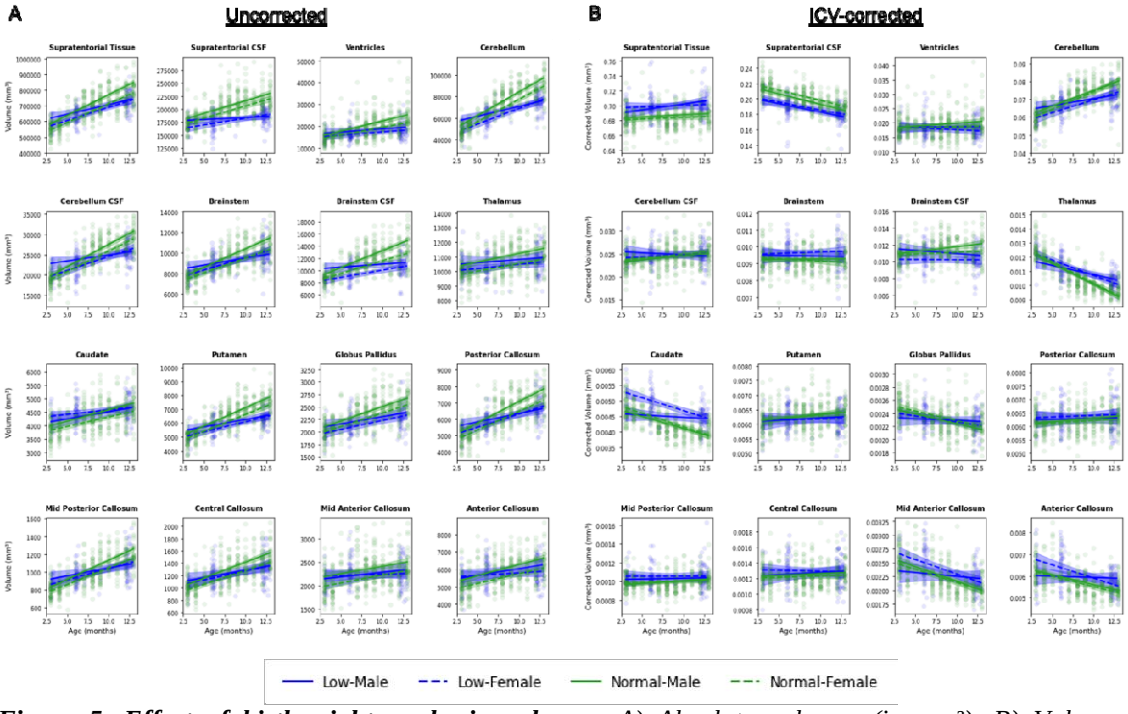

Figure 5. Effect of birthweight on brain volumes. *A) Absolute volumes (in mm³). B) Volumes corrected for ICV. The datapoints represent individual measurements. Each line represents the group means. Shaded areas indicate the 95% confidence interval for each group.*

Table 5. Summary results of the mixed-effects models assessing the effect of birthweight on brain volumes.

Uncorrected								
Region	**Group Effect**	**Corrected p (Group)**	**Age Effect**	**Corrected p (Age)**	**Age x Group Interaction Effect**	**Corrected p (Age x Group Interaction)**	**Sex Effect**	**Corrected p (Sex)**
Supratentorial tissue	1.25E+04	1.00E+00	1.49E+04	**1.49E-100**	9.65E+03	**1.40E-51**	4.91E+04	**4.91E-18**
Supratentorial CSF	1.87E+04	**4.30E-17**	1.77E+03	**7.77E-04**	2.98E+03	**2.03E-06**	9.38E+03	**5.13E-07**
Ventricles	1.33E+03	5.30E-02	2.98E+02	9.09E-02	4.66E+02	**8.06E-04**	2.09E+03	**2.31E-09**
Cerebellum	5.57E+03	**2.95E-08**	2.46E+03	**6.19E-123**	1.71E+03	**5.47E-21**	5.65E+03	**1.46E-13**
Cerebellum CSF	6.88E+02	9.18E-02	5.33E+02	**6.70E-17**	5.07E+02	**1.94E-16**	1.26E+03	**2.85E-10**
Brainstem	2.29E+01	1.00E+00	1.88E+02	**1.02E-25**	1.40E+02	**5.72E-19**	5.95E+02	**2.74E-10**
Brainstem CSF	1.14E+03	**3.42E-10**	1.89E+02	**1.29E-06**	3.06E+02	**1.35E-10**	1.27E+03	**1.74E-27**
Thalamus	6.50E+01	1.00E+00	5.26E+01	**3.31E-16**	6.26E+01	**7.97E-21**	6.00E+02	**1.75E-14**
Caudate	2.44E+02	**1.09E-05**	4.58E+01	**4.48E-11**	2.92E+01	**5.43E-12**	1.75E+02	**1.47E-04**
Putamen	3.48E+02	**2.61E-05**	1.36E+02	**3.39E-29**	1.08E+02	**1.47E-08**	3.96E+02	**1.71E-10**
Globus pallidus	1.01E+02	**2.09E-04**	3.43E+01	**1.26E-07**	1.93E+01	5.85E-02	1.06E+02	**8.91E-07**
Posterior callosum	1.40E+02	1.00E+00	1.35E+02	**1.64E-14**	9.93E+01	**1.31E-10**	4.51E+02	**6.48E-14**
Mid-posterior callosum	-1.88E+00	1.00E+00	2.25E+01	**1.62E-13**	1.68E+01	**8.56E-06**	5.77E+01	**1.59E-07**
Central callosum	4.12E+00	1.00E+00	2.78E+01	**2.04E-24**	1.75E+01	**3.57E-23**	9.51E+01	**3.33E-08**
Mid-anterior callosum	-3.23E+01	1.00E+00	1.31E+01	**3.96E-04**	1.84E+01	**1.55E-02**	1.51E+02	**1.21E-07**
Anterior callosum	-1.29E+02	1.00E+00	5.25E+01	**9.10E-03**	7.20E+01	**6.90E-03**	4.09E+02	**3.81E-09**
ICV-corrected								
Supratentorial tissue	-1.40E-02	**2.82E-26**	8.93E-04	1.38E-01	-5.63E-04	1.00E+00	2.55E-03	**3.85E-02**
Supratentorial CSF	1.25E-02	**1.43E-40**	-2.08E-03	**1.87E-12**	-3.43E-04	1.00E+00	-4.00E-03	**2.40E-05**
Ventricles	5.33E-04	1.00E+00	-7.24E-05	1.00E+00	1.76E-04	1.00E+00	8.02E-04	1.22E-01

Cerebellum	2.32E-03	**7.24E-03**	1.19E-03	**6.18E-14**	6.70E-04	**1.21E-03**	9.37E-04	**4.65E-02**
Cerebellum CSF	-2.90E-04	1.00E+00	3.58E-05	1.00E+00	1.56E-04	3.50E-01	-3.32E-04	3.71E-01
Brainstem	-3.37E-04	**1.28E-11**	-4.63E-06	1.00E+00	3.32E-06	1.00E+00	-3.87E-05	1.00E+00
Brainstem CSF	6.87E-04	**3.68E-17**	-2.14E-05	1.00E+00	1.20E-04	**1.70E-02**	5.17E-04	**1.41E-05**
Thalamus	-2.30E-04	**2.29E-10**	-1.81E-04	**9.35E-21**	-1.10E-04	**2.89E-06**	-1.23E-04	9.72E-01
Caudate	-3.87E-04	**8.89E-24**	-5.13E-05	**3.45E-07**	-3.12E-05	**3.52E-02**	-1.28E-04	**6.53E-11**
Putamen	1.07E-04	3.19E-01	1.60E-05	9.21E-01	8.50E-06	1.00E+00	-2.85E-05	1.00E+00
Globus pallidus	2.93E-05	1.00E+00	-1.19E-05	1.97E-01	-1.79E-05	**1.06E-02**	-4.93E-05	**8.18E-05**
Posterior callosum	-1.11E-04	2.92E-01	7.16E-06	1.00E+00	6.67E-06	1.00E+00	2.74E-05	1.00E+00
Mid-posterior callosum	-4.56E-05	**8.16E-09**	1.47E-06	1.00E+00	2.46E-06	1.00E+00	-1.08E-05	1.00E+00
Central callosum	-4.73E-05	9.11E-02	2.22E-06	1.00E+00	-7.30E-07	1.00E+00	1.10E-05	1.00E+00
Mid-anterior callosum	-9.92E-05	**1.63E-05**	-3.51E-05	**9.91E-07**	-1.54E-05	6.06E-01	-2.53E-06	1.00E+00
Anterior callosum	-3.16E-04	**3.99E-06**	-7.28E-05	**2.98E-05**	-1.29E-05	1.00E+00	1.82E-05	1.00E+00

Quantitative comparison of segmentation volumes between high-field and ULF MRI

Figure 6 shows that ventricles, cerebellum, putamen, and supratentorial tissue all have correlations above 0.8, indicating that changes in HF volumes are also captured in ULF segmentations. Thalamus and caudate also show relatively strong correlation between HF and ULF volumes, with coefficients above 0.75, while the correlation is weakest for globus pallidus with a coefficient of 0.62. Looking at the corrected percentage errors, supratentorial tissue, thalamus, caudate and globus pallidus all have mean CPE values close to zero, signifying that HF and ULF volumes are on the same scale. In contrast to this, the other regions have mean CPE values shifted from zero, revealing a systematic bias in ULF predictions, particularly visible for ventricles, with a mean CPE of –111%. When examining CPE in conjunction with correlation, supratentorial tissue, thalamus, caudate and ICV show both high correlation and low absolute CPE values, implying that the estimated volumes are on the same scale and that shifts in volumes are reflected similarly in both HF and ULF volumes.

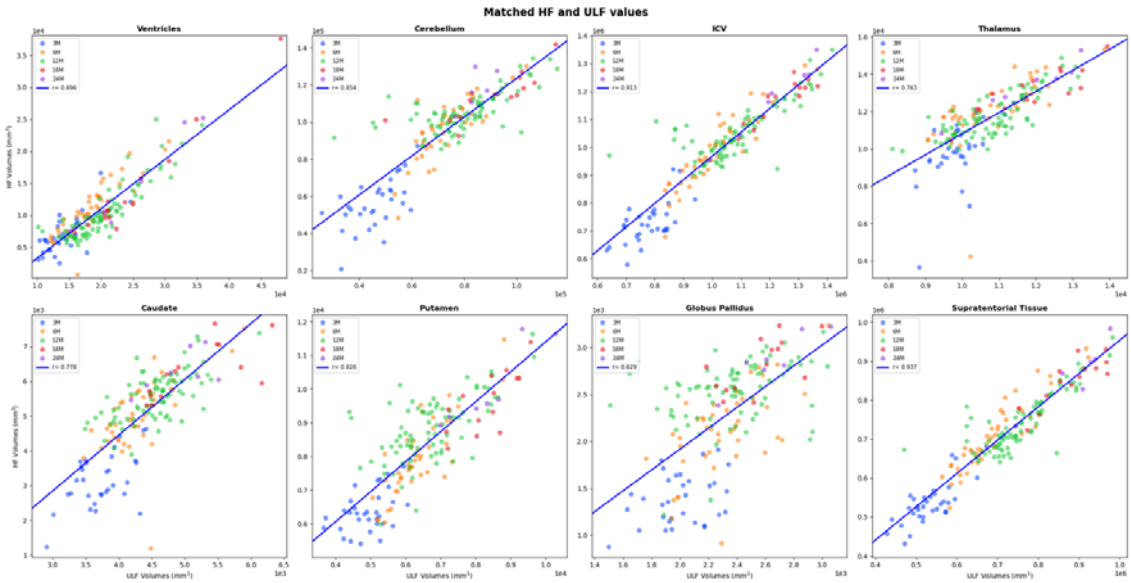

Figure 6: *Matched volume estimates in mm^3 for HF and ULF stratified by region and age. The blue line shows linear regression line computed using HF estimates as dependent variables and ULF estimates as independent variables.*

miniMORPH performance between cohorts

Results for matched segmentations were compared between the Uganda-PRIMES and UCT-Khula cohorts. As Uganda-PRIMES only had matched scans at 12 months, the comparison was done between Uganda-PRIMES and UCT-Khula for 12-month-old subjects only. Table 6 shows significant differences in CPE between cohorts for cerebellum, thalamus, putamen, globus pallidus and ICV ($p<0.05$). Interestingly, the difference between ICV and cerebellum is significant, while supratentorial tissue is not significantly different, indicating that one of the major drivers for ICV difference between cohorts is related to difference in cerebellum estimation between 1.5T T1 and 3T T2w. Cohort differences are also visible in figure 7 which shows that that Uganda-PRIMES has a wider CPE distribution for all regions except globus pallidus and that UCT-Khula has a higher precision. Correspondingly, table 7 shows that correlations for all regions are higher for UCT-Khula showing that the linear correspondence between HF and ULF is stronger for the UCT-Khula cohort.

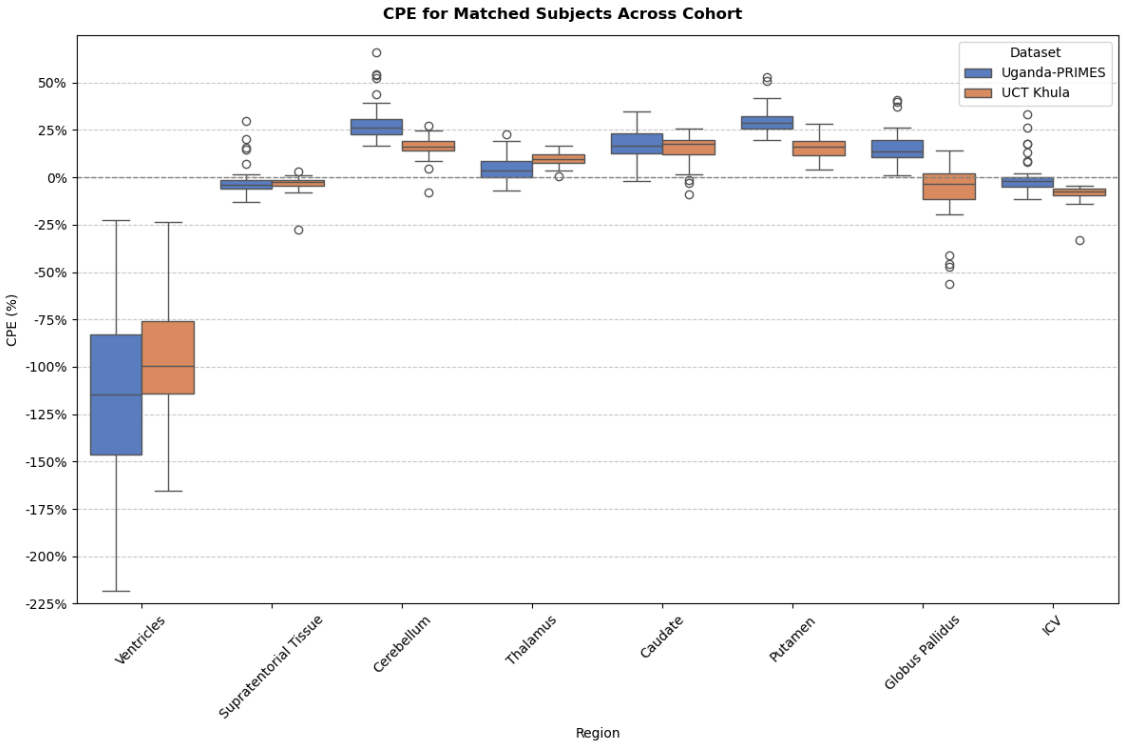

Figure 7: CPE estimates 12 months old subjects stratified by cohort and region. Boxes *show interquartile range with median CPE represented as middle line.*

Region	**Uganda-PRIMES Mean CPE (%)**	**UCT-Khula Mean CPE (%)**	**p-value**
Ventricles	-113.346	-97.211	0.091
Supratentorial Tissue	-2.119	-3.545	0.285
Cerebellum	29.247	16.035	0.000
Thalamus	4.921	9.874	0.000
Caudate	17.184	15.309	0.646
Putamen	29.887	15.771	0.000
Globus Pallidus	15.688	-6.766	0.000
ICV	0.147	-8.341	0.000

Table 6: Mean CPE for Uganda-PRIMES and UCT-Khula with corresponding p-values, testing for significant difference between cohorts. *Significance testing was done using two sided Mann-Whitney U Test.*

Region	**UCT-Khula**	**Uganda-PRIMES**
Ventricles	0.913	0.816
Cerebellum	0.867	0.404
ICV	0.928	0.292
Thalamus	0.937	0.610
Caudate	0.756	0.499

Putamen	0.876	0.495
Globus Pallidus	0.586	0.573
Supratentorial Tissue	0.926	0.404

Table 7: Spearman's rank correlation for each matched ROI, stratified by cohort.

miniMORPH performance at different ages

A comparison of miniMORPH performance across ages was done including both UCT-Khula and Uganda-PRIMES subjects. Figure 8 shows that the spread of CPE is largest at 3 months for all regions, indicating that there is an increased random error at 3 months. This spread also corresponds to the low correlation between HF and ULF volumes for 3 months old subjects shown in figure 8. It is worth noting that the coefficient of variance (sigma/μ) for HF is also larger, indicating that HF results have a larger variance between subjects when compared to other ages. Most regions have similar performance in terms of correlation and CPE for 6, 12 and 18 months. At 24 months, although a decrease in correlation is observed, the low sample makes performance estimates uncertain.

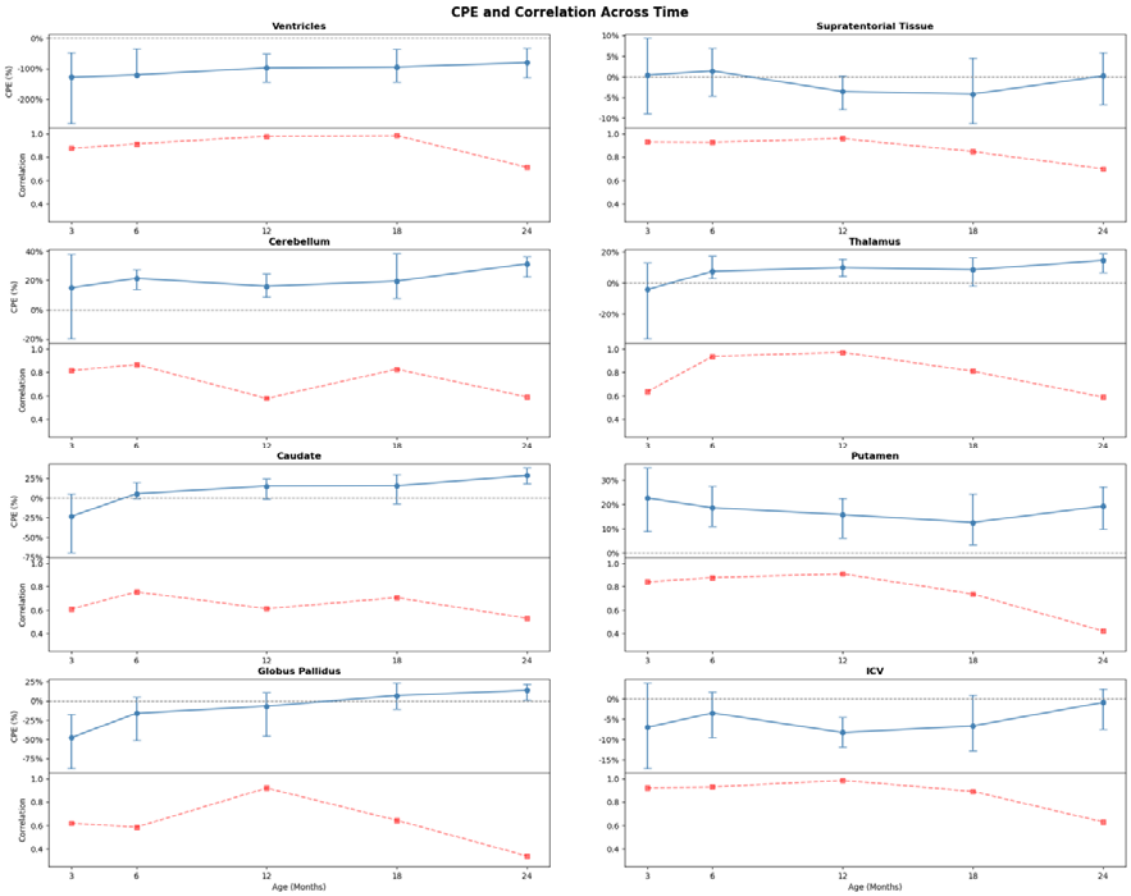

Figure 8: CPE and Spearman's rank correlation coefficient for matched UCT-Khula subjects, stratified by age.

4. Discussion

In this work, we introduced miniMORPH, a scalable, fully automated pipeline for extracting brain morphometry from ULF MRI data acquired in infancy. Despite the inherent challenges associated with low spatial resolution and contrast of ULF data acquired during infancy (Abate et al., 2024), miniMORPH reliably segmented major brain structures, tracking developmental trajectories across multiple brain regions.

Specifically, the pipeline successfully captured significant age-related volumetric changes in both supratentorial and infratentorial regions, as well as subcortical nuclei such as the caudate and putamen. Notably, these effects remained significant for many structures after ICV correction, suggesting the pipeline is sensitive not only to global brain growth but also to region-specific maturational changes. The inclusion of non-linear age terms further highlighted the pipeline's capacity to resolve developmental acceleration and deceleration phases typical of early infancy (Dean et al., 2014). Together, these results demonstrate that miniMORPH achieves biologically meaningful segmentation of ULF data, enabling robust volumetric analyses during a critical window of brain development.

In addition to age effects, robust sex-related differences were evident across widespread brain regions in the uncorrected data, with males generally exhibiting larger volumes in structures such as supratentorial tissue, the cerebellum, and posterior corpus callosum (Gilmore et al., 2007; Knickmeyer et al., 2014). However, following correction for ICV, most of these differences were substantially attenuated, indicating that much of the observed variance was attributable to overall head size rather than regional specialisation. The residual sex effects that remained significant after ICV correction were subtle and largely restricted to CSF spaces and select subcortical structures. This suggests that global scaling effects drive much of the apparent sexual dimorphism in neonatal brain volumes, with few brain region specific differences persisting after normalisation. Overall, these findings are consistent with previous evidence that volume-normalised comparisons reveal few significant sex differences in early life (Holland et al., 2014; Knickmeyer et al., 2014).

We also show that miniMORPH can detect meaningful group-level differences in brain development associated with early-life risk factors, such as low birthweight. Significant effects of birthweight group were observed across multiple brain regions. In uncorrected models, children born with low birthweight exhibited increased CSF volumes and reduced tissue volumes in regions including the supratentorial compartment, cerebellum, caudate, and putamen. After ICV correction, birthweight differences persisted in selected regions—notably the cerebellum and caudate—indicating localised volumetric alterations independent of global brain size. Age-by-group interaction effects were also identified in structures such as the cerebellum, thalamus, and corpus callosum, suggesting divergent developmental trajectories associated with birthweight. These findings support the validity of the automated processing pipeline used in this analysis and underscore the potential of miniMORPH for early identification of infants at risk for adverse outcomes—particularly in settings where HF imaging and long-term follow-up may not be feasible. Nevertheless, it should be noted that birthweight is confounded with acquisition site in this proof-of-concept analysis. Future work should aim to replicate and refine these findings in harmonised, multi-site cohorts.

Investigating the CPE results shows a deviation in mean CPE values, especially prominent in the ventricles. One explanation for this is that SynthSeg and miniMORPH are different algorithms based on different labels. Specifically, while miniMORPH uses infant-specific labels, the current version of SynthSeg is trained on adult labels. This difference might generate a systematic shift by dilating or eroding segmented areas. Another explanation—particularly relevant for the ventricles—relates to the acquisition sequence used for ULF scans. All ULF data were acquired using T2-weighted sequences, where CSF appears hyperintense. The combination of this increased CSF signal, lower SNR, and reduced spatial resolution may lead to an overestimation of ventricular volume, especially in participants with narrow ventricles. Such apparent ventricular enlargement would result in a negative CPE, which aligns with our observed findings.

When stratifying by cohort, both correlation and CPE analyses revealed differences between UCT-Khula and Uganda-PRIMES sites. Specifically, the UCT-Khula cohort showed consistently higher correlations across all regions, along with CPE values significantly closer to zero for the cerebellum, caudate and globus pallidus.

A primary hypothesis for this discrepancy relates to scanner differences. Participants at the Uganda-PRIMES site were scanned on a 1.5T MRI system while those in the UCT-Khula cohort were scanned on a 3T scanner. The lower magnetic field strength at Uganda-PRIMES likely results in reduced SNR, potentially increasing the level of unstructured noise and reducing the reliability of comparisons with ULF segmentation outputs. It also must be noted that, as Uganda-PRIMES subjects were scanned using a T1-weighted sequence, segmenting areas bordering to CSF might have been more challenging due to lower contrast between CSF and GM. Finally, another driver of these differences might be the fact that both Uganda-PRIMES and UCT-Khula subjects were registered to templates created using UCT-Khula subjects. Although the same ULF sequence and scanner were used for both cohorts, there might be unknown demographic, technical, or procedural differences, resulting in differences in the scans. Such cohort-specific differences might also be propagated to the template, making it more tailored towards the dataset it is derived from. Therefore, registering Uganda-PRIMES scans to a UCT-Khula derived template might produce a larger registration error. Combined, the difference in magnetic field strength, sequence, and the template effect are likely causing performance differences between Uganda-PRIMES and UCT-Khula cohorts.

Importantly, differences in miniMORPH performance across sites and developmental stages suggest that segmentation precision is modulated by both data quality and underlying anatomical maturity. Specifically, accuracy was lower in scans acquired at younger ages and in higher-motion datasets—conditions that are particularly prevalent at 3 months of age. Temporal analysis of segmentation performance revealed markedly increased CPE variance at this age across all regions, indicating a heightened degree of uncertainty in volumetric estimates early in development.

This variability likely stems from both neurodevelopmental and technical factors. Anatomically, the grey–white matter (GM/WM) boundaries are less well defined between 3 and 9 months in particular, due in large part to limited and spatially-variable myelination, resulting in poor tissue contrast on both HF and ULF images. The reduced contrast at this

stage challenges both convolutional segmentation approaches, such as those used in SynthSeg (Li et al., 2019), and registration-based pipelines like miniMORPH, making accurate tissue classification more difficult and increasing the likelihood of segmentation errors. This uncertainty is not confined to ULF imaging; similar variability is observed in HF data at the same age, reflected by an increased coefficient of variation in regional volumes.

Moreover, the sources of segmentation error in HF and ULF images are largely uncorrelated, as each modality is influenced by different imaging properties (e.g., SNR, spatial resolution, and sequence-dependent contrast). As a result, this uncorrelated noise propagates into the CPE measure—defined as the difference between HF and ULF segmentations—thereby amplifying overall variance. This issue is further exacerbated by the standardisation step in CPE calculation, which involves dividing by HF volumes. Since smaller regions yield smaller denominators, this normalisation step introduces proportionally greater variability in regions with low absolute volume, especially in early infancy.

The globus pallidus consistently exhibited poorer segmentation performance, a finding that can likely be attributed to several interrelated factors. First, its relatively small size means that even minor absolute segmentation errors can lead to disproportionately large relative errors, particularly when metrics such as CPE are normalised by HF volumes. This mirrors the challenges observed more generally at 3 months of age, where lower anatomical contrast and smaller regional volumes contribute to inflated variance in error estimates.

Second, the internal border of the globus pallidus is especially difficult to resolve in infant MRI due to inherently low GM-WM contrast in this region, particularly in early infancy before substantial myelination has occurred. While some variation in contrast across the structure may be present, such as subtle differentiation between internal (GPi) and external (GPe) segments, this is often inconsistent and not reliably discernible on ULF or conventional MRI at this age, limiting accurate parcellation. Additionally, the globus pallidus contains high concentrations of iron (Hallgren & Sourander, 1958), which enhances contrast at high field strengths but is far less visible at lower field, further complicating segmentation accuracy in low-field settings.

Third, unlike many cortical and ventricular regions, the globus pallidus does not border CSF, which typically provides a strong contrast boundary that aids tissue discrimination. The absence of this neighbouring high-intensity reference region further reduces boundary definition and segmentation precision.

Lastly, although large CPE values suggest considerable discrepancy between HF and ULF estimates in this region, the correlation between modalities remains moderate. This implies that while the volumes differ in absolute terms, the relative ordering across individuals is preserved to some extent—highlighting that segmentation uncertainty here may be systematic rather than random. These observations suggest that caution is warranted when interpreting globus pallidus volumes from ULF data, and that further optimisation may be needed to improve reliability in this structure.

In summary, this study demonstrates that miniMORPH is a robust and scalable pipeline capable of extracting biologically meaningful morphometric information from ULF MRI

acquired in early infancy. Despite the inherent limitations of ULF imaging—namely lower resolution, SNR and contrast—miniMORPH successfully segmented major brain regions and detected age- and sex-related volumetric changes consistent with known developmental trajectories. Crucially, the pipeline was sensitive to region-specific maturational patterns even after correcting for ICV, highlighting its ability to capture both global and localized neurodevelopmental dynamics. Furthermore, miniMORPH identified significant structural differences associated with early-life risk factors such as low birthweight. These findings underscore the pipeline's potential for early risk stratification in resource-constrained or longitudinally limited settings where HF imaging is not feasible.

Importantly, comparison with HF-derived segmentations provided a benchmark for assessing the validity and reliability of ULF-derived measures. Regions such as supratentorial tissue, which showed both high correlation and low mean CPE, were highly comparable across scanners, supporting the feasibility of using miniMORPH for cross-platform longitudinal studies or integration with existing HF-based growth charts. In contrast, regions like the ventricles, while showing strong correlations, exhibited systematic biases in absolute volume—likely arising from modality-specific signal differences and segmentation boundary challenges. These biases can, however, be addressed through linear correction models, enabling more meaningful comparison between HF and ULF-derived metrics.

Taken together, these findings establish miniMORPH as a practical and effective tool for enabling large-scale, early-life neurodevelopmental studies using ULF imaging. It bridges a critical methodological gap by allowing robust volumetric analysis in contexts where traditional HF neuroimaging is infeasible, thereby advancing efforts toward more equitable and accessible pediatric brain health monitoring. The pipeline is openly available at https://github.com/UNITY-Physics/fw-minimorph.

5. Funding

This work was funded by the Bill and Melinda Gates Foundation (INV-018164, INV-005774, INV-047888 and INV-047885). The work in South Africa was supported by Wellcome LEAP 1kD programme (The First 1000 Days) [222076/Z/20/Z].

6. Acknowledgements

The authors thank the caregivers, families, and infants in South Africa and Uganda who made this work possible. We would also like to acknowledge the Khula South Africa and Uganda data collection and data management team for the many hours that went into acquiring the data used in manuscript. SW would like to thank the National Institute for Health and Care Research (NIHR) Maudsley Biomedical Research Centre (BRC) for their ongoing support of KCL neuroimaging facilities.

7. References

Abate, F., Adu-Amankwah, A., Ae-Ngibise, K., Agbokey, F., Agyemang, V., Agyemang, C., Akgun, C., Ametepe, J., Arichi, T., Asante, K., Balaji, S., Baljer, L., Basser, P., Beauchemin, J., Bennallick, C., Berhane, Y., Boateng-Mensah, Y., Bourke, N., Bradford, L., … Williams, S. (2024). UNITY: A low-field magnetic resonance neuroimaging initiative to characterize neurodevelopment in low and middle-income settings. *Developmental Cognitive Neuroscience*, *69*, 101397. https://doi.org/10.1016/j.dcn.2024.101397

Avants, B. B., Tustison, N. J., Wu, J., Cook, P. A., & Gee, J. C. (2011). An open source multivariate framework for n-tissue segmentation with evaluation on public data. *Neuroinformatics*, *9*(4), 381–400. https://doi.org/10.1007/S12021-011-9109-Y

Billot, B., Greve, D. N., Puonti, O., Thielscher, A., Van Leemput, K., Fischl, B., Dalca, A. V., Iglesias, J. E., & ADNI. (2023). SynthSeg: Segmentation of brain MRI scans of any contrast and resolution without retraining. *Medical Image Analysis*, *86*, 102789. https://doi.org/10.1016/j.media.2023.102789

Bruchhage, M. M. K., Ngo, G.-C., Schneider, N., D'Sa, V., & Deoni, S. C. L. (2020). Functional connectivity correlates of infant and early childhood cognitive development. *Brain Structure & Function*, *225*(2), 669. https://doi.org/10.1007/s00429-020-02027-4

Chen, L., Wu, Z., Hu, D., Wang, Y., Zhao, F., Zhong, T., Lin, W., Wang, L., & Li, G. (2022). A 4D infant brain volumetric atlas based on the UNC/UMN baby connectome project (BCP) cohort. *NeuroImage*, *253*, 119097. https://doi.org/10.1016/j.neuroimage.2022.119097

de Kieviet, J. F., Zoetebier, L., van Elburg, R. M., Vermeulen, R. J., & Oosterlaan, J. (2012). Brain development of very preterm and very low-birthweight children in childhood and adolescence: A meta-analysis. *Developmental Medicine and Child Neurology*, *54*(4), 313–323. https://doi.org/10.1111/j.1469-8749.2011.04216.x

Dean, D. C., O'Muircheartaigh, J., Dirks, H., Waskiewicz, N., Lehman, K., Walker, L., Han, M., & Deoni, S. C. L. (2014). Modeling healthy male white matter and myelin development: 3 through 60 months of age. *NeuroImage*, *84*, 742–752. https://doi.org/10.1016/j.neuroimage.2013.09.058

Deoni, S. C., Bruchhage, M. M., Beauchemin, J., Volpe, A., D'Sa, V., Huentelman, M., & Williams, S. C. (2021). Accessible pediatric neuroimaging using a low field strength MRI scanner. *Neuroimage*, *238*, 118273.

Deoni, S. C. L., O'Muircheartaigh, J., Ljungberg, E., Huentelman, M., & Williams, S. C. R. (2022). Simultaneous high□resolution T2□weighted imaging and quantitative T 2 mapping at low magnetic field strengths using a multiple TE and multi□orientation acquisition approach. *Magnetic Resonance in Medicine*, *88*(3), 1273–1281. https://doi.org/10.1002/mrm.29273

Desikan, R. S., Ségonne, F., Fischl, B., Quinn, B. T., Dickerson, B. C., Blacker, D., Buckner, R. L., Dale, A. M., Maguire, R. P., Hyman, B. T., Albert, M. S., & Killiany, R. J. (2006). An automated labeling system for subdividing the human cerebral cortex on MRI scans into gyral based regions of interest. *NeuroImage*, *31*(3), 968–980. https://doi.org/10.1016/j.neuroimage.2006.01.021

Donnay, C., Okar, S. V., Tsagkas, C., Gaitán, M. I., Poorman, M., Reich, D. S., & Nair, G. (2024). Super resolution using sparse sampling at portable ultra-low field MR. *Frontiers in Neurology*, *15*, 1330203. https://doi.org/10.3389/fneur.2024.1330203

Gilmore, J. H., Lin, W., Prastawa, M. W., Looney, C. B., Vetsa, Y. S. K., Knickmeyer, R. C., Evans, D. D., Smith, J. K., Hamer, R. M., Lieberman, J. A., & Gerig, G. (2007). Regional gray matter growth, sexual dimorphism, and cerebral asymmetry in the neonatal brain. *The Journal of Neuroscience: The Official Journal of the Society for Neuroscience*, *27*(6), 1255–1260. https://doi.org/10.1523/jneurosci.3339-06.2007

Hallgren, B., & Sourander, P. (1958). The effect of age on the non□haemin iron in the human brain. *Journal of Neurochemistry*, *3*(1), 41–51.

Hoffmann, M., Hoopes, A., Greve, D. N., Fischl, B., & Dalca, A. V. (2024). Anatomy-aware and acquisition-agnostic joint registration with SynthMorph. *Imaging Neuroscience (Cambridge, Mass.)*, *2*, 1–33. https://doi.org/10.1162/imag_a_00197

Holland, D., Chang, L., Ernst, T. M., Curran, M., Buchthal, S. D., Alicata, D., Skranes, J., Johansen, H., Hernandez, A., Yamakawa, R., Kuperman, J. M., & Dale, A. M. (2014). Structural

Growth Trajectories and Rates of Change in the First 3 Months of Infant Brain Development. *JAMA Neurology*, *71*(10), 1266–1274. https://doi.org/10.1001/jamaneurol.2014.1638

Hoopes, A., Mora, J. S., Dalca, A. V., Fischl, B., & Hoffmann, M. (2022). SynthStrip: Skull-stripping for any brain image. *NeuroImage*, *260*, 119474. https://doi.org/10.1016/j.neuroimage.2022.119474

Jenkinson, M., Beckmann, C. F., Behrens, T. E. J., Woolrich, M. W., & Smith, S. M. (2012). FSL. *NeuroImage*, *62*(2), 782–790. https://doi.org/10.1016/J.NEUROIMAGE.2011.09.015

Knickmeyer, R. C., Wang, J., Zhu, H., Geng, X., Woolson, S., Hamer, R. M., Konneker, T., Styner, M., & Gilmore, J. H. (2014). Impact of sex and gonadal steroids on neonatal brain structure. *Cerebral Cortex (New York, N.Y.: 1991)*, *24*(10), 2721–2731. https://doi.org/10.1093/cercor/bht125

Li, G., Wang, L., Yap, P.-T., Wang, F., Wu, Z., Meng, Y., Dong, P., Kim, J., Shi, F., Rekik, I., Lin, W., & Shen, D. (2019). Computational neuroanatomy of baby brains: A review. *NeuroImage*, *185*, 906–925. https://doi.org/10.1016/j.neuroimage.2018.03.042

Rutherford, S., Fraza, C., Dinga, R., Kia, S. M., Wolfers, T., Zabihi, M., Berthet, P., Worker, A., Verdi, S., & Andrews, D. (2022). Charting brain growth and aging at high spatial precision. *Elife*, *11*, e72904.

Sabir, H., Kipfmueller, F., Bagci, S., Dresbach, T., Grass, T., Nitsch-Felsecker, P., Pantazis, C., Schmitt, J., Schroeder, L., & Mueller, A. (2023). Feasibility of bedside portable MRI in neonates and children during ECLS. *Critical Care*, *27*(1), 134.

Schwarz, G. (1978). Estimating the Dimension of a Model. *The Annals of Statistics*, *6*(2), 461–464. https://doi.org/10.1214/aos/1176344136

Song, L., Peng, Y., Ouyang, M., Peng, Q., Feng, L., Sotardi, S., Yu, Q., Kang, H., Sindabizera, K. L., Liu, S., & Huang, H. (2024). Diffusion□tensor□imaging 1□year□old and 2□year□old infant brain atlases with comprehensive gray and white matter labels. *Human Brain Mapping*, *45*(7), e26695. https://doi.org/10.1002/hbm.26695

Tu, D., Goyal, M. S., Dworkin, J. D., Kampondeni, S., Vidal, L., Biondo-Savin, E., Juvvadi, S., Raghavan, P., Nicholas, J., & Chetcuti, K. (2023). Automated analysis of low-field brain MRI in cerebral malaria. *Biometrics*, *79*(3), 2417–2429.

Walhovd, K. B., Fjell, A. M., Brown, T. T., Kuperman, J. M., Chung, Y., Hagler, D. J., Roddey, J. C., Erhart, M., McCabe, C., Akshoomoff, N., Amaral, D. G., Bloss, C. S., Libiger, O., Schork, N. J., Darst, B. F., Casey, B. J., Chang, L., Ernst, T. M., Frazier, J., … Gruen, J. (2012). Long-term influence of normal variation in neonatal characteristics on human brain development. *Proceedings of the National Academy of Sciences*, *109*(49), 20089–20094. https://doi.org/10.1073/pnas.1208180109